tion; the thinner films and the films with lower carrier concentration, respectively, have superior sensitivity.

Conclusions

Tin oxide films were prepared in the temperature range from 300 to 700°C by CVD method using direct oxidation of $SnCl_4$. Electrical properties of the films were largely affected by deposition temperature. As deposition temperature increased from 300 to 500°C, film resistivity decreased to $\sim 3 \times 10^{-3}$ Ω-cm, but a further increase of the temperature to 700°C caused a rapid increase in film resistivity. It was found from Hall measurement that this trend was attributed mainly to carrier concentration rather than carrier mobility. It is concluded that the donor electrons are probably a result of chlorine incorporation into the lattice during the deposition process, with the high resistivity of the 700°C film caused by less Cl content due to the easy decomposition of Sn—Cl bond at high temperature. The sensitivity of SnO_2 films to reducing gases, such as H_2 and LPG, was greater in the thinner film and in films with lower carrier concentration.

Manuscript submitted Oct. 18, 1990; revised manuscript received April 5, 1991.

Pusan National University assisted in meeting the publication costs of this article.

REFERENCES

1. K. L. Chopra, S. Major, and D. K. Pandya, *Thin Solid Films*, **102**, 1 (1983).
2. H. Pink, L. Treitinger, and L. Vité, *Jpn. J. Appl. Phys.*, **19**, 513 (1980).
3. R. B. Cooper, G. N. Advani, and A. G. Jordan, *J. Electron. Mater.*, **10**, 455 (1981).
4. S. C. Chang and D. B. Hicks, "Transducer '85," International Conference on Solid-State Sensors and Actuators, p. 381 (1985).
5. T. Oyabu, Y. Ohta, and T. Kurobe, *Sensors and Actuators*, **9**, 301 (1986).
6. V. Demarne and A. Grisel, "Transducer '87," International Conference on Solid-State Sensors and Actuators, p. 605 (1987).
7. Z. M. Jarzebski and J. P. Marton, *This Journal*, **123**, 199 (1976).
8. C. A. Vincent, *ibid.*, **119**, 515 (1972).
9. J. A. Aboaf, V. C. Marcotte, and N. J. Chou, *ibid.*, **120**, 701 (1973).
10. K. B. Sundaram and G. K. Bhagavat, *J. Phys. D*, **14**, 333 (1981).
11. E. Shanthi, V. Dutta, A. Banerjee, and K. L. Chopra, *J. Appl. Phys.*, **51**, 6243 (1981).
12. O. Tabata, in "Chemical Vapor Deposition," J. M. Blocher, Jr., H. E. Hintermann, and L. H. Hall, Editors, p. 681, The Electrochemical Society Softbound Proceedings Series, Pennington, NJ (1975).
13. K. Adachi and M. Mizuhashi, in "Chemical Vapor Deposition," G. W. Cullen and J. M. Blocher, Jr., Editors, PV 87-8, p. 999, The Electrochemical Society Softbound Proceedings Series, Pennington, NJ (1987).
14. H. Windischmann and P. Mark, *This Journal*, **126**, 627 (1979).
15. N. Yamamoto, S. Tonomura, T. Matsuoka, and H. Tsubomura, *Jpn. J. Appl. Phys.*, **20**, 721 (1981).
16. G. N. Advani and A. G. Jordan, *J. Electron. Mater.*, **9**, 29 (1980).

Morphology and Electrochemical Effects of Defects on Highly Oriented Pyrolytic Graphite

R. S. Robinson*

Bellcore, Navesink Research and Engineering Center, Red Bank, New Jersey 07701

Kent Sternitzke, Mark T. McDermott, and Richard L. McCreery*

Department of Chemistry, The Ohio State University, Columbus, Ohio 43210

ABSTRACT

Highly oriented pyrolytic graphite (HOPG) has been studied by several groups as an electrode material, due mainly to its well-defined surface structure compared to more commonly used materials such as glassy carbon. The basal plane of HOPG is also a common standard for scanning tunneling microscopy because it is atomically flat over regions up to at least 10^4 A^2 and is generally free of gross microstructural defects. Thus, HOPG serves well as a nearly perfect single-crystal surface for studies of the chemical properties of basal plane sp^2 carbon. In previous reports on laser activation of HOPG, it was demonstrated that electrode capacitance, electron transfer kinetics, and Raman spectrum depend on laser-induced disorder, particularly edge plane defects. The present work was undertaken to describe surface defects on HOPG at the STM level for two grades of HOPG and the laser-activated surface. Capacitance, k^o for $Fe(CN)_6^{-3/-4}$, and anthraquinone disulfonate adsorption all correlate with the presence of STM observable defects. In addition, STM of the laser-activated surface is consistent with a damage mechanism driven by thermal expansion. The results confirm the importance of edge plane defects to the electrochemical behavior of carbon electrodes.

Highly oriented pyrolytic graphite has been studied by several groups as an electrode material (1-8), due mainly to its well-defined surface structure compared to more commonly used materials such as glassy carbon (GC). The basal plane of HOPG is a common standard for scanning tunneling microscopy (STM) (9-13) because it is atomically flat over regions up to at least 10^4 A^2 and is generally free of gross microstructural defects. Thus, HOPG serves well as a nearly perfect single-crystal surface for studies of the chemical properties of basal plane sp^2 carbon. Electrochemical properties of HOPG and related materials have been reviewed (14-17).

It was established quite early that the HOPG basal plane has an anomalously low capacitance in electrolyte solution of 1.5-3 μF cm^{-2}, compared to 15-30 for typical metals and >50 μF cm^{-2} for edge plane carbon (3-7). Due to the large difference between basal and edge plane capacitance, the observed capacitance for a laser-damaged HOPG surface is dependent on the fraction of edge planes created by the laser radiation (3). Important details of the mechanism of oxidation-induced damage to HOPG have been revealed by Raman spectroscopy (1, 2) and STM (3). In addition, heterogeneous electron transfer on HOPG has been shown to be strongly dependent on the presence of graphitic edge planes for several redox systems, with the rate constant (k^o) on edges being $\sim 10^5$ times faster than on basal planes for $Fe(CN)_6^{-3/-4}$ (1, 3). All of these phenomena have been associated with defects on an otherwise perfect basal plane. Since the capacitance and k^o are much higher for edge *vs.* basal plane graphite, the observed capacitance and kinetics on HOPG are controlled largely by edge plane defects. For example, since k^o for an edge plane is 10^5 that for basal, 1% defect density causes an increase in the observed rate constant of a factor of 10^3. Spectroscopic, scanning electron microscopy (SEM), and STM results imply that electrochemical oxidation of HOPG leads to large damaged re-

* Electrochemical Society Active Member.

gions which appear to nucleate at defects on the surface (1, 2, 11). Since oxidation would be expected to be more rapid at edge plane defects, it is likely that lattice damage begins at the defect, then grows to cover larger areas as oxidation ensues.

These observations indicate the electrochemical importance of defects on HOPG and by implication to a variety of graphite materials. However, the results of Raman spectroscopy and electrochemical methods depend on the spatial average of the surface properties on a distance scale much larger than the defects. The purpose of the present work is to investigate the surface morphology of HOPG and laser-damaged HOPG at the STM level (nm-μm scale.) The appearance of surface defects will then be correlated with electrochemical observations to provide insight into the structural basis of electron transfer, adsorption, and capacitance. In addition, the mechanism of laser-induced defect generation will be considered. Of particular importance to the approach is a large zoom ratio for the STM, which was achieved with a custom instrument employing both hardware and software zooms.

Experimental

The STM used here differs substantially from earlier published descriptions (13, 18, 19) and from commercial instruments. The xyz translator was a bend-polarized tube (10) with a coaxially mounted tube for z-translation (18) (Fig. 1). The displacement sensitivity of the STM scanner to applied voltages was determined with several methods (13). Images were recorded with the scanner moving in both directions of the x and y scans. This is less convenient than recording in one direction and discarding the back scans, which are distorted by scanner creep (as are the forward scans), but allows evaluation of thermal drift and tip asymmetry or contamination. The images shown here have been corrected for scanner creep (20). The amount of correction varied with the scan area, from 2 to 15% for scans from 400 nm to 4.5 μm. A 32 bit microcomputer (Apple Macintosh II with MacAdios II interface, GW Instruments) and two (640 × 480 and 1024 × 768 pixels) 256-color monitors were used for STM control and image display. The scan generator circuit (Fig. 1) dynamically optimized the scan rate for surface roughness (18), minimizing image acquisition time on surfaces with a wide range of roughness. For smooth surfaces, the scan proceeded at the maximum rate, and scan rates as high as 0.4 mm s^{-1} have been obtained, permitting acquisition of a 4 × 4 μm, 730 × 730 pixel image in ~15 s. The scanning and image display software allowed a large-area (up to 4.5 × 4.5 μm) survey scan to be performed, with interactive zooming to an area of interest.

For scanning, the sample was clamped in the STM and electrical contact was made with silver paint. The tip bias was +55 mV and the tunneling current 2-3 nA (constant-current mode.) The tips were made from 250 μm $Pt_{0.8}Ir_{0.2}$ wire (Longreach Scientific, Pt-010-30-R). The graphite samples were type "ZYA" and "ZYH" HOPG (Union Carbide, Parma, Ohio) and were cleaved with adhesive tape before scanning. The graphite samples are graded by the manufacturer according to x-ray diffraction linewidth, where the linewidth is inversely proportional to the a axis coherence length, L_a. L_a is a measure of average in-plane microcrystallite size. ZYA grade has a linewidth of 0.4 ± 1° and L_a of >1 μm, while ZYH has a linewidth of 3.5°.

For most voltammetry and capacitance measurements, the electrode area was defined by an O-ring as described previously (3), and the diffusional area was determined by chronoamperometry of $Fe(CN)_6^{-3/-4}$. For capacitance and k^o measurements, ZYA and ZYH basal planes were immersed in electrolyte within 1 min of cleaving, and electrochemical experiments were conducted within 1 min of immersion. It was noted that the voltammetric ΔE_p increased with time when a fresh surface was exposed to air, with a maximum reached in 30-60 min. For this reason, fresh surfaces were immersed as quickly as allowed by the cell design preceding capacitance and electrode kinetic measurements (about 1 min). Capacitance was determined with a 10 mV triangle wave potential waveform as described by Gileadi (21, 22) and reported by us previously (3). Linear sweep voltammetry was conducted under computer control of a function generator and A/D converter. Capacitance measurements and $Fe(CN)_6^{-3/-4}$ voltammetry were conducted in 2*M* KCl, while anthraquinone-2,6 disulfonate (AQDS) was studied in 0.1*M* $HClO_4$. In order to minimize mechanical strain on the HOPG, several adsorption experiments were conducted with a wall-less, inverted drop cell. The freshly cleaved surface was mounted on a sheet metal contact with graphite/nujol paste, and a drop of electrolyte solution was placed on the basal plane surface. After completing the circuit with a Pt auxiliary and Pt quasi-reference electrode, voltammograms were determined conventionally. AQDS adsorption was determined after 10 min of adsorption from a 1.0×10^{-5}*M* solution in 0.1*M* $HClO_4$.

Laser activation with a Nd:YAG (1064 nm) laser was carried out in air as described previously (1, 3) at both 55 and 105 MW cm^{-2}, as noted below. A small N_2 laser (337 nm) was also used in several cases, with the beam attenuated by metal apertures and focused onto the HOPG with a 10X microscope objective (23). Based on the laser spot size measured with an optical microscope and the attenuated beam power, the N_2 laser activation averaged 67 MW cm^{-2} over a ~22 μm radius spot.

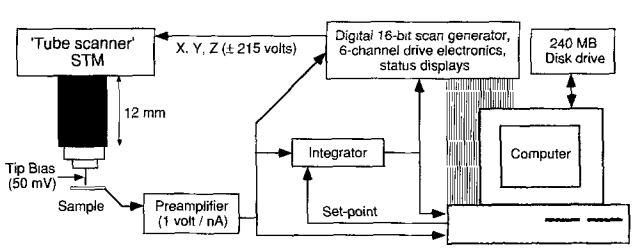

Fig. 1. Schematic diagram of STM. All images were acquired in air.

Results

A series of gray-scale images of the surface of untreated ZYA grade HOPG is shown in Fig. 2 and 3. The gray shading is keyed to tip displacement; all features in the images were stable over a 24 h observation period. Figure 2A is a 3 × 4 μm survey scan of HOPG showing several defects which include the ribbon-like feature at upper right and steps running diagonally across the image near the top and bottom of the image. Regions of the image examined in greater detail in Fig. 3a-f are indicated by the rectangles. Figure 3A shows a variety of structures apparently caused by the folding of the strip-like fragment of graphite which is on the surface. Figures 3B-E are higher magnification views showing other types of features contained in this structure. The twin stylus-like defect that appears to project from the end of the feature in Fig. 3D (see contrast-enhanced region) spans the length of the entire strip-like defect (Fig. 3B, C); the other end is shown in greater detail in Fig. 3E. The dual ridges appear to emanate from the step edge. Figure 3E is shown in quasi-three-dimensional perspective, with a line scan showing the approximate 15 Å height of the ridges. This image represents the maximum resolution of the STM in the configuration used in these experiments (for wide scan area), which did not permit observation of atomic-scale corrugation.

Figures 2 and 3 illustrate three general types of defects on the ZYA sample studied here. The ribbon-like defects of Fig. 3A-C are relatively uncommon and may result from mechanical damage during cleaving. The step edges of Fig. 2B and 3F are common, with one or two apparent on a typical 2 × 2 μm scan. The height of these step edges varied from less than 7 to more than 50 Å. Finally, the "ridge" of Fig. 3E was observed occasionally, but its origin is not clear. Since large areas of the ZYA surface were not examined and their defects were not catalogued, the relative densities of various defect types are necessarily semiquantitative.

As noted in the Experimental section, ZYH-grade HOPG has larger x-ray diffraction linewidths and smaller microcrystallites than ZYA. As shown in Fig. 4, ZYH exhibits

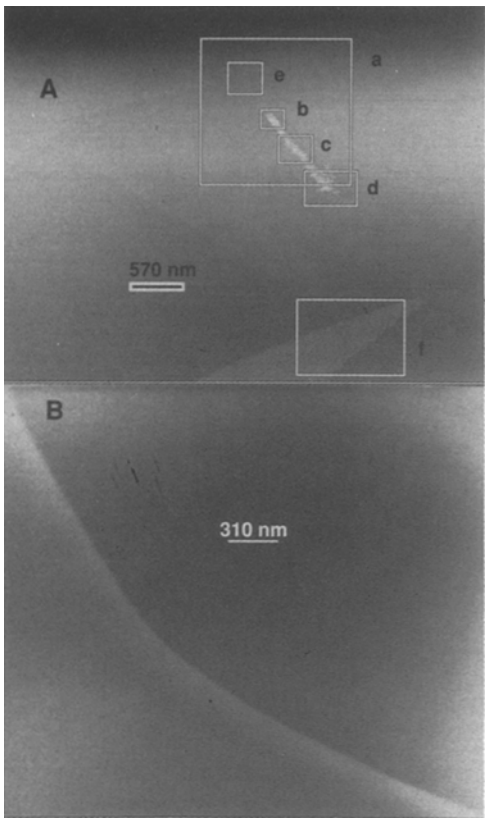

Fig. 2. (A) 4 × 3 μm STM image of untreated ZYA-grade HOPG basal plane. The outlined areas are shown in more detail in Fig. 3. The total gray scale range is 26 nm; white areas are higher. Image B is a scan of a different region of the ZYA surface. B is more typical than A, with the outlined defects in A being relatively uncommon. A least squares fitted plane was subtracted from the images to eliminate effects of sample tilt and improve contrast. The gray scale range in B is 10.2 nm.

numerous step edge defects. The line scan across the ZYH surface shows step heights in the range of 10-60 Å, significantly larger and more frequent than those on ZYA-grade HOPG. A close-up of ZYH (Fig. 5) shows both a 27 Å high step edge and a "valley" 22 Å deep and ~500 Å wide. The Raman spectra of ZYA and ZYH basal plane exhibited no 1360 cm^{-1} band, implying that the edge plane density is

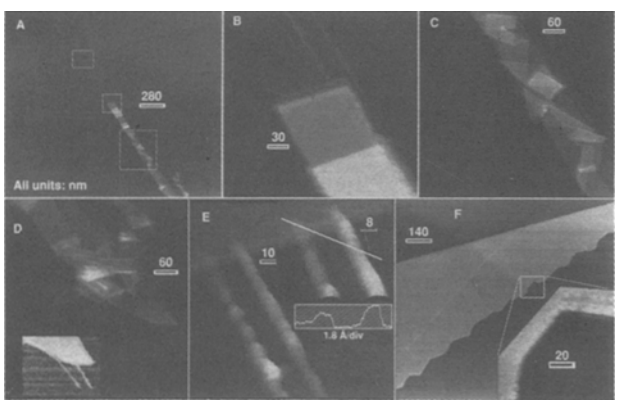

Fig. 3. Images A-F are closeups of regions labeled in Fig. 2A. The x-y scale is given in each image, in units of nm. All images are shown in flat gray scale viewed normal to the surface, except E which is a quasi-three-dimensional rendition viewed 45° relative to the surface normal. B, C, and E correspond to boxes in A. The gray scale is keyed to tip displacement; the gray scale ranges are 200, 160, 190, 300, 50, and 66 Å for A-F, respectively. The inset figures in E and F have gray scale ranges of 33 and 34.5 Å. The inset in D has been enhanced in contrast through statistical differencing to improve detail. A fitted plane was subtracted from A and F.

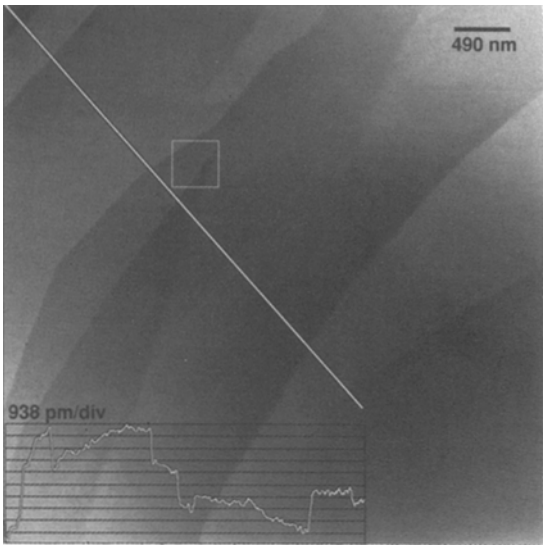

Fig. 4. Low-resolution STM image of ZYH basal plane, same conditions as Fig. 2. Inset shows line scan along the line indicated on the image. The outlined area is shown in greater detail in Fig. 5A. The gray scale range is 29.3 nm, and a fitted plane was subtracted.

much lower than laser-activated HOPG, and too low to be detectable by Raman spectroscopy (1). Figures 5A-B show line-profiles and histograms of regions adjacent to step edges on ZYH and ZYA basal planes. Based on the histogram of Fig. 5B, the height of the step on ZYA is 6.76 ± 0.2 Å, while the line scan yields 6.6 Å. Since the interplanar spacing of HOPG is 3.354 Å, the step edge of Fig. 5B corresponds to two graphite layers. Single-layer

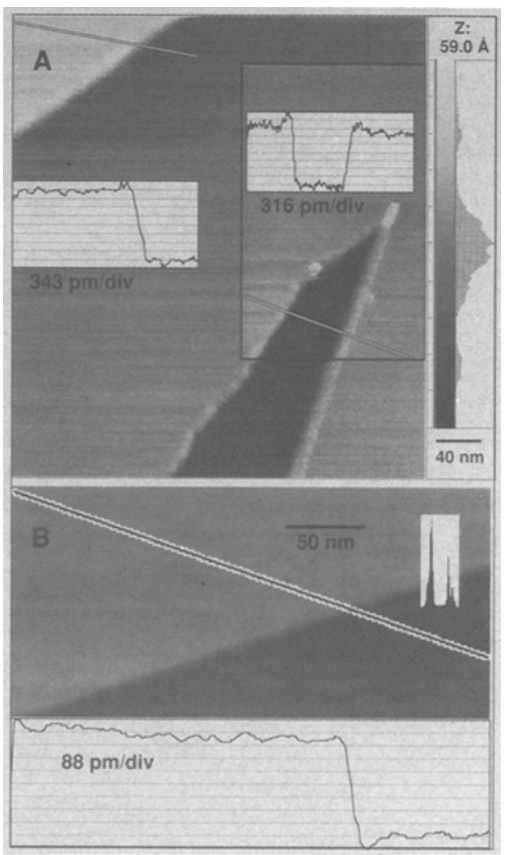

Fig. 5. Line scans and histograms across close-ups of defects of HOPG. A is on ZYH HOPG, B is on ZYA. A is a magnified portion of the upper left of Fig. 4. The gray scale range from white to black in B is 29.5 nm (only a portion of the entire image is shown.) B was smoothed with a 3 × 3 pixel moving average window and a fitted plane was subtracted.

Table I. Electrochemical parameters of ZYA and ZYH basal plane.

	°C ($\mu F/cm^2$)	ΔE_p $Fe(CN)_6^{-3/-4}$ 0.1 V/s[a] (mV)	k^o (cm/s)	Γ^b AQDS ($pmol/cm^2$)
ZYA	2.05 ± 0.25 (N = 10)	680 ± 52 (N = 10)	9×10^{-6}	20 ± 7 (N = 5)
ZYH	2.56 ± 0.31 (N = 11)	480 ± 100 (N = 10)	7×10^{-5}	37 ± 8 (N = 5)
Laser-activated ZYA, 55 MW/cm^2	5.2 ± 0.8 (N = 5)	68 ± 3 (N = 5)	0.019	
Laser-activated ZYA, 105 MW/cm^2	25.3 ± 2.2 (N = 5)	71 ± 2 (N = 5)	0.015	
Laser-activated ZYH, 105 MW/cm^2	27.1 ± 2.5 (N = 5)	76 ± 4 (N = 5)	0.010	

[a] 2M KCl, voltammogram acquired *ca.* 1 min after cleaving.
[b] Determined in 0.1M $HClO_4$, $10^{-5}M$ AQDS, inverted drop cell.

step defects have been observed for HOPG treated in air at elevated temperature (12).

The electrochemical characteristics of ZYA and ZYH basal planes were compared to assess the effects of defects on capacitance, electron transfer kinetics, and adsorption. Since the defect density is likely to vary significantly for different cleaved surfaces, there is variation in electrochemical properties from surface to surface. For some (~20%) cases, freshly cleaved HOPG exhibited small ΔE_p (less than 100 mV) for $Fe(CN)_6^{-3/-4}$ or double voltammetric peaks apparently due to high defect density (3). These cases were not included in averaged capacitance or k^o data. Figure 6 shows representative voltammograms of $Fe(CN)_6^{-3/-4}$ on ZYH and ZYA basal surfaces. Table I lists the average capacitance and ΔE_p for $Fe(CN)_6^{-3/-4}$ on the two materials, and results on laser-activated HOPG are included for comparison. We reported previously that graphitic edge planes have much higher capacitance than basal planes (70 *vs.* 2 $\mu F/cm^2$) and higher k^o for $Fe(CN)_6^{-3/-4}$ (0.1 *vs.* $<10^{-7}$ cm s^{-1}) (3). In addition, the observed C^o and k^o values for laser-activated HOPG were consistent with a sum of the basal and edge values, weighted according to fractional surface area. Assuming this model is correct, ZYH would be expected to have higher C^o_{obs} and smaller ΔE_p than ZYA due to the higher defect density evident in the STM images. Although the results are consistent with the model, the picture is clouded somewhat by the run-to-run variation for a series of surfaces from the same graphite sample.

A more dramatic consequence of defects is apparent when studying adsorption of anthraquinone 2,6-disulfonate (AQDS). AQDS is known to adsorb on platinum, with an apparent molecular area of 131 Å (24), and it has a quasi-reversible voltammetric wave centered at 0.01 V *vs.* Ag/AgCl in 1M $HClO_4$ (24). AQDS adsorption has also been studied in detail on Hg, with saturation coverage occurring at concentrations below $10^{-6}M$ (25). The voltammogram of AQDS on ZYA basal plane is shown in Fig. 7A. ΔE_p is very large, implying small k^o, but the peak current is linear with $\nu^{1/2}$, as expected for a diffusion-controlled redox process. Thus, AQDS adsorption on ZYA is not apparent by voltammetry at 0.3 V/s, at least for 1 mM solutions. AQDS appears to be a well-behaved, nonadsorbing, albeit kinetically slow redox system on ZYA basal plane. Figure 7B is a voltammogram for AQDS on ZYH under the same conditions. The sharp, reversible couple centered at −0.05 V *vs.* Ag/AgCl has a peak current which is linear with ν (Fig. 8), implying it is caused by adsorbed AQDS. The adsorption peak obeys a Langmuir-type isotherm at low concentration, with a peak width of 50 mV. Its behavior is quite different at 1 mM concentration from the sharp voltammetric spike observed on mercury (25). The couple in Fig. 7B with large ΔE_p is similar to that observed on ZYA, with a linear peak current dependence on $\nu^{1/2}$. Quantitative results for AQDS adsorption are listed in Table I, with Γ_{AQDS} determined from the area of the voltammetric adsorption peak and the geometric drop area. Despite significant run-to-run variation, ZYA grade exhibits a lower average Γ_{AQDS} than ZYH.

As noted in Table I and several previous reports, intense laser pulses delivered to HOPG *in situ* greatly increased k^o_{obs} and to a smaller extent C^o_{obs} (1). As demonstrated by Raman spectroscopy and SEM, the laser pulse damages the basal plane to form numerous microcrystallites, with dimensions in the hundreds of Angstrom range. The increased edge density in the laser-damaged region is re-

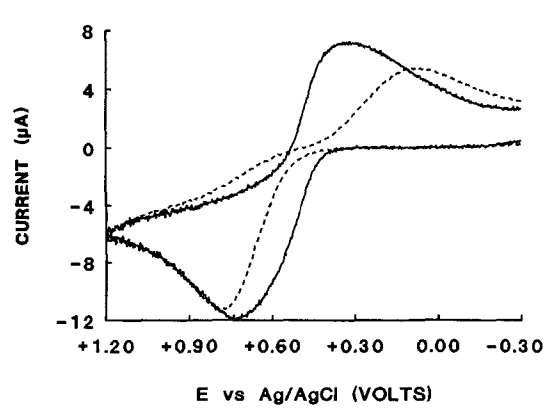

Fig. 6. Voltammograms of 1 mM $Fe(CN)_6^{-3/-4}$ in 2M KCl at 0.1 V/s on ZYA and ZYH basal planes. Dashed line is ZYA, solid line is ZYH.

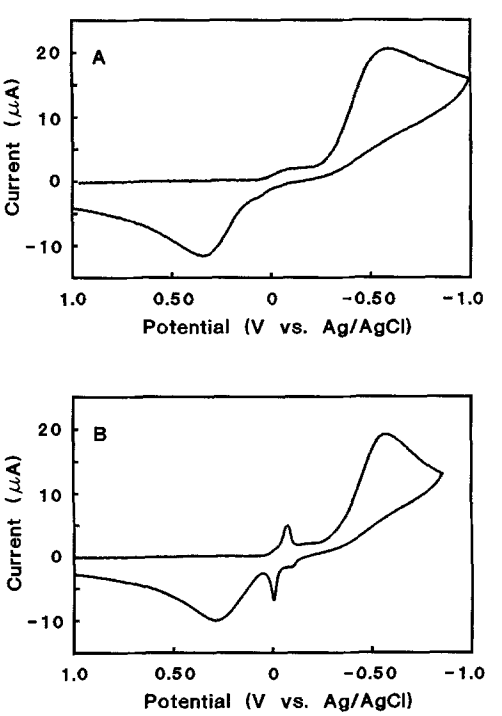

Fig. 7. Voltammograms of 1 mM AQDS in 0.1M $HClO_4$, 0.3 V s^{-1} on ZYA (curve A) and ZYH (curve B) basal plane.

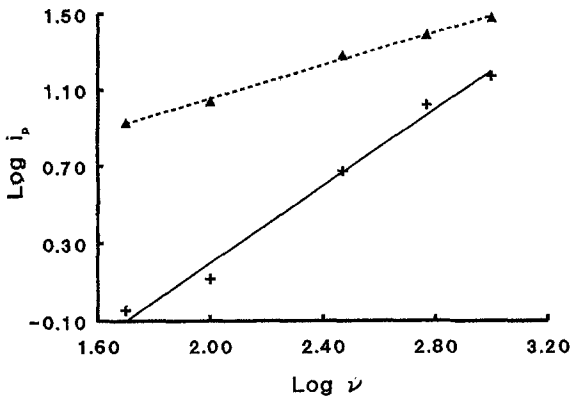

Fig. 8. Peak current vs. scan rate, on log-log scale, for peak at −0.55 V vs. Ag/AgCl (triangles) and at −0.1 V vs. Ag/AgCl (pulses) for voltammogram of AQDS on ZYH, similar to Fig. 7B. Slope of upper line is 0.45; slope of lower line is 1.0. Scan rate units are mV s^{-1}, current units are μA.

sponsible for the increased k^o_{obs} and C^o_{obs} and these two parameters may be quantitatively correlated (3). Figure 9 shows STM images of HOPG following Nd:YAG (55 MW cm^{-2}) and N_2 (67 MW cm^{-2}) exposures. The vertical height distribution of the images is 100-300 Å; the basal plane surface is obviously severely disrupted by the laser exposure. Although differences in laser damage for the two lasers might be expected due to wavelength, power density, and pulse duration, these variables were not examined in detail. The images of Fig. 9 are not sufficient to conclude any major difference between the effects of the two different lasers. Figure 10 is a STM image of the edge of a N_2 laser-damaged spot. The disrupted region is higher than the undisturbed basal plane by about 200 Å, indicating that the laser has formed a plateau rather than a crater.

Discussion

As is clear from Fig. 2-5, the nature and density of surface defects depend on both the type of HOPG and its preparation. Stated differently, the x-ray coherence length, L_a, correlates inversely with the surface defect density for ZYA and ZYH HOPG samples. Thus, the material with smaller L_a (ZYH) has a higher density of defects and greater surface and bulk disorder than ZYA. Extensive experience with cleaving HOPG samples emphasizes the extreme care required to avoid surface damage of a fresh basal plane surface. As concluded previously based on capacitance and kinetic results, relatively little damage to the surface can dramatically affect basal plane properties (3). Presumably random defects introduced during cleaving are responsible for the significant statistical variation in C^o_{obs} and k^o_{obs} for both ZYA and ZYH samples. It should also be noted that the HOPG grade affects the ability to cleave a visually "perfect" surface with ZYH generally yielding more macroscopic defects. With the inverted drop "cell," it was observed that these visual defects were much more active to both AQDS adsorption and $Fe(CN)_6^{-3/-4}$ electron transfer.

As noted by Gerisher (26) and Yeager *et al.* (4-7) the anomalously low capacitance of undamaged basal plane may be due to the low density of electronic states predicted for graphite crystals. It is possible that the low k^o observed on basal plane may be due to the same phenomenon, but there is little available evidence to distinguish this possibility from other mechanisms based on hydrophobic effects, specific adsorption, etc. It is clear from the present work that the influence of defects on both capacitance and k^o must be considered carefully when interpreting basal plane phenomena.

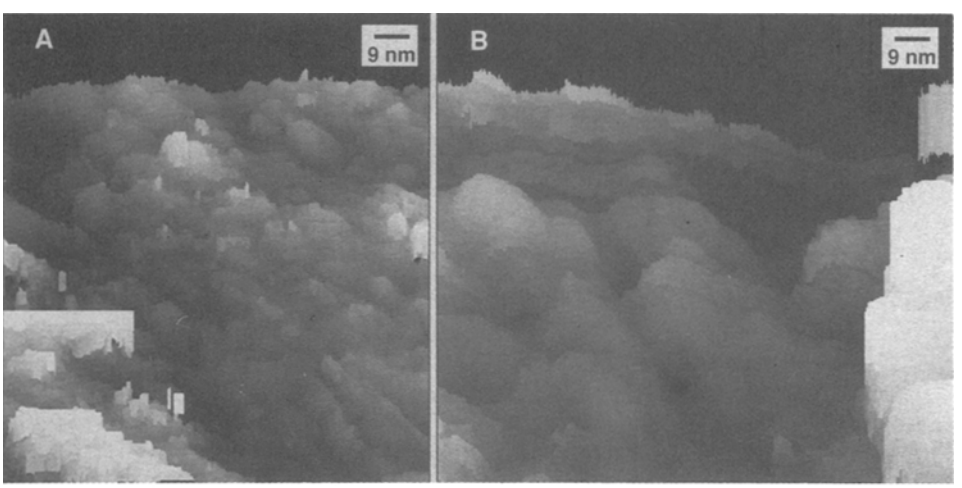

Fig. 9. STM image of ZYA HOPG after laser irradiation in air. Image A is after three 67 MW cm^{-2} N_2 laser pulses; B is after three 55 MW cm^{-2} Nd:YAG laser pulses. The peak-to-peak amplitude (gray scale range) is 12.9 nm (A) and 70.5 nm (B). Both were median-filtered with a 3 × 3 pixel window.

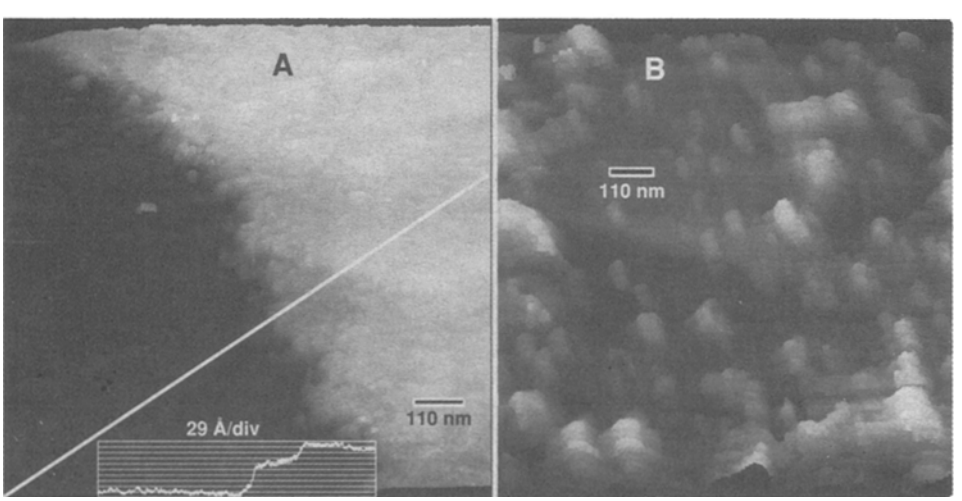

Fig. 10. STM image of edge of laser-damaged region: (A) N_2 and (B) YAG. The gray scale range is 45 nm (A) and 102 nm (B). B was median-filtered with a 3 × 3 pixel window.

The slightly higher capacitance of ZYH is expected from the higher fractional edge plane density (f_e). Based on the assumption that C^o_{obs} is a weighted sum of edge and basal capacitance, f_e is about 0.8% for ZYH. Similarly, k^o for ZYH is higher than ZYA due to higher f_e. Since $\sqrt{Dt}$ at 0.1 V/s is large compared to the spacing of defects, k^o_{obs} is a weighted sum of edge and basal contributions. f_e calculated from k^o_{obs} is about 0.1%. The reason for the disagreement with the capacitance results is not clear but may be due to the nonideality of the voltammogram apparent in Fig. 6. As noted in the Experimental section, k^o_{obs} decreased with the time of air exposure between cleaving the HOPG and immersion in electrolyte. This effect is probably due to impurity adsorption on residual defects on the HOPG, and it was minimized by quick immersion and rapid measurement of freshly cleaved basal plane surfaces. In previous reports (1, 3), a larger ΔE_p was reported for $Fe(CN)_6^{-3/-4}$ and a longer time elapsed before immersion in solution. Nevertheless, the capacitance and kinetic results are consistent with a low density of edge plane defects distributed on the basal plane, with a higher average density of ZYH than for ZYA.

The voltammograms for AQDS are consistent with strong adsorption to edge plane sites and weak adsorption on basal planes. Furthermore, electron transfer is much faster for the adsorbed AQDS, thus confirming the anisotropy of rate on HOPG observed for other redox systems (1-8, 12). Although AQDS adsorption on HOPG was not observed directly (*e.g.*, with STM), the adsorption correlates with defect density assessed by other methods. Thus, x-ray results, STM, capacitance, k^o_{obs}, and AQDS adsorption all indicate higher surface defect density for ZYH over ZYA. However, it is clear that sample preparation and handling can introduce as much variation in defect density as the inherent HOPG grade, and that preparation of low defect surfaces required extreme care. When run-to-run variations are averaged, the results reveal the correlation of surface defects with HOPG type.

It is possible that the laser pulse could have caused either the plateau or the crater in Fig. 10, since it was not possible to image the entire laser spot with the STM. The conclusion that the laser causes a plateau is based on the greater roughness observed on the uplifted region. This conclusion is consistent with a thermally driven damage mechanism. The c axis thermal expansion coefficient of 23×10^{-6}/°C is at least 20 times larger than the a axis value. As the laser heats the HOPG surface, the lattice will expand, even though the surrounding unirradiated region remains relatively cool. As shown schematically in Fig. 11, thermal expansion will introduce strain during or just after the laser pulse, which apparently causes lattice damage when a threshold is exceeded. The damaged material does not settle back to its original condition after the laser pulse, resulting in the plateau. This mechanism was also concluded regarding HOPG damage by a more energetic laser pulse, and higher fluence can lead to melting (26). Given that several thousand laser pulses produce a crater in GC (27-29), the damage mechanisms may be quite different for HOPG and GC.

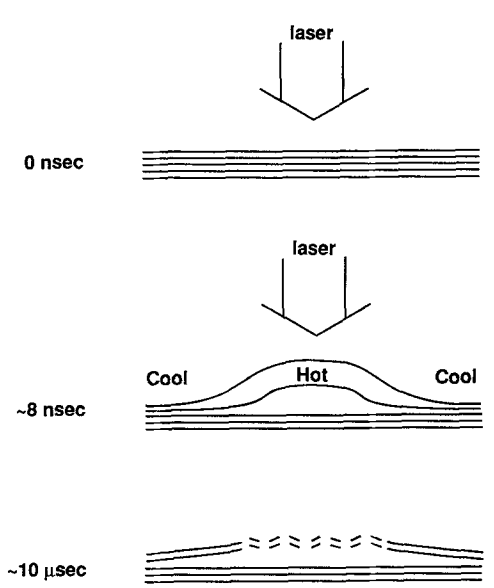

Fig. 11. Possible mechanism for laser damage of HOPG based on thermal expansion. Graphite planes are viewed along the a axis.

In conclusion, it is clear that capacitance, $Fe(CN)_6^{-3/-4}$ redox kinetics, and AQDS adsorption on HOPG are dominated by edge plane defects on the surface, because all three variables differ greatly on edge *vs.* basal plane. Although the present results are mainly semiquantitative, they do provide information about the morphology and density of such defects on ZYA and ZYH graphite. It is also important to note that surface defect density varies with sample preparation and handling, in addition to the inherent microstructural order. As stated earlier, laser activation causes significant damage and defect creation on HOPG, and the mechanism probably involves differential thermal expansion or melting. Since k^o for $Fe(CN)_6^{-3/-4}$ is so much higher on edge planes than basal planes, rate enhancement is much more dependent on edge plane creation than on increased microscopic surface area.

Acknowledgment

The work at The Ohio State University was supported by AFOSR Grant No. 88-0071. The authors are grateful to A. Gozdz and P. L. Key for helpful comments on the manuscript.

Manuscript submitted Nov. 16, 1990; revised manuscript received March 25, 1991.

Bellcore assisted in meeting the publication costs of this article.

REFERENCES

1. R. Bowling, R. Packard, and R. L. McCreery, *J. Am. Chem. Soc.*, **111,** 1217 (1989).
2. R. Bowling, R. T. Packard, and R. L. McCreery, *Langmuir*, **5,** 683 (1989).
3. R. J. Rice and R. L. McCreery, *Anal. Chem.*, **61,** 1637 (1989).
4. I. Morcos and E. Yeager, *Electrochim. Acta*, **15,** 953 (1970).
5. J. P. Randin and E. Yeager, *J. Electroanal. Chem.*, **36,** 257 (1972).
6. J. P. Randin and E. Yeager, *This Journal*, **118,** 711 (1971).
7. J. P. Randin and E. Yeager, *J. Electroanal. Chem.*, **58,** 313 (1975).
8. R. M. Wightman, E. C. Paik, S. Borman, and M. A. Dayton, *Anal. Chem.*, **50,** 1410 (1978).
9. C. Binnig, H. Rohrer, E. Gerber, and E. Weibel, *Phys. Rev. Lett.*, **49,** 57 (1982).
10. G. Binnig and D. P. E. Smith, *Rev. Sci. Instrum.*, **57,** 1688 (1986).
11. A. A. Gewirth and A. J. Bard, *J. Phys. Chem.*, **92,** 5563 (1988).
12. H. Chang and A. J. Bard, *J. Am. Chem. Soc.*, **112,** 4598 (1990).
13. R. S. Robinson, *This Journal*, **136,** 3145 (1989).
14. K. Kinoshita, "Carbon: Electrochemical and Physicochemical Properties," John Wiley & Sons, New York (1988).
15. J. P. Randin, in "Encyclopedia of Electrochemistry of the Elements," Vol. 7, A. J. Bard, Editor, pp. 1-291, Marcel Dekker, New York (1976).
16. J. O. Besenhard and H. P. Fritz, *Angew. Chem., Int. Ed.*, **22,** 950 (1983).
17. R. L. McCreery, in "Electroanalytical Chemistry," Vol. 17, A. J. Bard, Editor, Marcel Dekker, New York (1990).
18. R. S. Robinson, *J. Microsc.*, **152 Pt2,** 541 (1988).
19. R. S. Robinson, *J. Vac. Sci. Technol.*, **A8,** 511 (1990).
20. R. S. Robinson, *J. Comp. Assist. Microsc.*, **2,** 53 (1990).
21. E. Gileadi and N. Tshernikovski, *Electrochim. Acta*, **16,** 579 (1971).
22. E. Gileadi, N. Tshernikovski, and M. Babai, *This Journal*, **119,** 1018 (1972).
23. K. Sternitzke and R. L. McCreery, *Anal. Chem.*, In

press (1990).
24. M. P. Soriaga and A. T. Hubbard, *J. Am. Chem. Soc.*, **104,** 2735 (1982).
25. P. He, R. M. Crooks, and L. R. Faulkner, *J. Phys. Chem.*, **94,** 1135 (1990).
26. H. Gerisher, *ibid.*, **89,** 4249 (1985).
27. J. Steinbeck, G. Braunstein, M. Dresselhaus, T. Venkatesan, and D. Jacobson, *J. Appl. Phys.*, **58,** 4374 (1985), and *ibid.*, **64,** 1802 (1988).
28. J. S. Speck, J. Steinbeck, G. Braunstein, M. S. Dresselhaus, and T. Venkatesan, in "Beam-Solid Interactions and Phase Transformations," Proceedings of the Materials Research Society, Pittsburgh, PA (1985).
29. J. S. Speck, J. Steinbeck, and M. S. Dresselhaus, *J. Mater. Res.*, In press (1990).
30. M. Poon and R. L. McCreery, *Anal. Chem.*, **60,** 1725 (1988).

Characteristics of Ultrafine Grain P53 Screens

Esther Sluzky*

Hughes Aircraft Company, Industrial Products Division, Carlsbad, California

Kenneth Hesse*

Consultant, Escondido, California

ABSTRACT

The brightness and resolution characteristics of P53 phosphor screens prepared by cataphoretic coating using a 0.9 μm average particle size powder are described and compared to sputtered and single-crystal screens as well as to 2.5 μm P53 screens. It is shown that the single-crystal and sputtered screens have spot size capabilities better than 0.17 mil (full wave half amplitude) compared to 0.25 mil for the 0.9 μm screens. However, brightness of the particulate screens is substantially superior (>40%) to the sputtered screens, which were better than single-crystal screens. Resolution was measured on the screen without the use of a complete tube assembly with its electron gun. Instead, contact printer technology, using a United States Air Force test pattern placed in contact with the screen, and an enlarged image made by transmitted light was viewed to select the just barely resolvable pattern.

This paper examines the possibilities of producing particulate screens having the capability of single-crystal and sputtered screens regarding resolution while having appreciably better light output. Several years ago, we described a method for evaluating the screen contribution to overall tube spot size (1, 2). A single-crystal screen consisting of a thin-film layer of epitaxially grown YAG:Tb P53 phosphor was fabricated into a high-resolution tube. Under these conditions the diameter of the electron-beam is reproduced by the luminescent light image. Making use of the findings reported, an overall tube design that can produce 50% linewidths of about 1 mil and slightly less was established using P53 phosphor of 2.5 μm average particle size. The screens were deposited by cataphoretic coating (3).

Experimental and Discussion

Recently, Hughes, using RF-sputtered, translucent P53 screens provided by Bell Laboratories (4), fabricated these screens into high-resolution tubes. In so doing, we had the opportunity to compare the light output and resolution performances of the single-crystal screen tubes, the particle screen tubes mentioned above, and the sputtered screen tubes. The screen characteristics are shown in Table I.

The screens consisted of seven cataphoretically coated P53 phosphor screens, with an average particle size (APS) of 2.5 μm on fiber optic substrates. Screen thickness was approximately 6 μm; there were five RF-sputtered phosphor screens, APS approximately 0.4 μm on sapphire substrates. Screen thickness was 1½-3 μm, and two epitaxially grown P53 films on single-crystal undoped YAG substrates. Screen thickness was 2-3 μm.

The test data obtained for these tubes is shown in Table II. The decreasing light output when going from a particulate screen structure, to the sputtered screen, and finally to the single-crystal screen can be seen. The single-crystal screen loses light out the sides of the thin film due to the light piping action of its high refractive index structure. The sputtered screen on the other hand, having a translucent structure due to its very fine crystallite size, prevents this light piping similar to a particulate screen. Light scattering in all directions occurs in the layer with subsequent increase in light output in the forward direction.

Table I. Screen data—particle, sputtered, and single-crystal screens.

Screen type	Average particle size (μm)	Screen thickness (μm)	Number of tubes	Substrate
Particle	2.5	6.0	7	Fiber optic
Sputtered	0.4	1.5-3	5	Sapphire
Crystal	N/A	2-3	2	YAG

The linewidth data show interesting insights into the resolution capabilities of phosphor screens. As stated previously, the single-crystal screen reproduces the beam diameter of the electron gun. Work done during the current investigation showed that the sputtered screens also reproduced the beam diameter. When we examine the linewidth data for the crystal and sputtered screens, it can be seen that the guns in these tubes were averaging 0.725 mils for their beam size and ranged from 0.56 to 0.93. Most of the guns would be acceptable for meeting the requirements of the tubes being built for a helmet-mounted, airborne display system (5). The only exceptions are those up at the high end of the range. When these guns are put into tubes having the 2.5 μm particulate screens it can be seen that the linewidth increases. The average is now at 1.00 mils and the range from 0.85 to 1.33. It should be noted that not all of this increase in linewidth was due to the screen. The fiber optic faceplates that the screens were deposited upon also degrade the beam linewidth because of their discrete structure.

Since it was known that the sputtered screens have a discrete crystallite pattern consisting of 0.4 μm particles and since the data shows the linewidth of sputtered and single-crystal screens to be essentially the same, it was decided to determine how closely ultrafine grain particulate screen performance could approach that of the sputtered layer.

The resolution of a tube is dependent upon a number of individual contributions as shown by the equation

$$d_t^2 = d_{co}^2 + d_{sph}^2 + d_{ast}^2 + d_{sc}^2 + d_s^2 + d_{ot}^2 \quad [1]$$

* Electrochemical Society Active Member.